UNIVERSITYOF BIRMINGHAM

Improving the interpretation of mercury porosimetry data using computerised X-ray tomography and mean-field DFT

Rigby, S.P.; Chigada, P.I.; Wang, J.; Wilkinson, S.K.; Bateman, H.; Al-Duri, B.; Wood, J.; Bakalis, S.; Miri, T.

Document Version
Publisher's PDF, also known as Version of record

[Link to publication on Research at Birmingham portal](#)

Improving the interpretation of mercury porosimetry data using computerised X-ray tomography and mean-field DFT

Sean P. Rigby [a,*], Peter I. Chigada [b], Jiawei Wang [c], Sam K. Wilkinson [c], Henry Bateman [c], Bushra Al-Duri [c], Joseph Wood [c], Serafim Bakalis [c], Taghi Miri [c]

[a] Department of Chemical and Environmental Engineering, University of Nottingham, University Park, Nottingham NG7 2RD, UK
[b] Department of Chemical Engineering, University of Bath, Claverton Down, Bath BA2 7AY, UK
[c] Centre for Formulation Engineering, Department of Chemical Engineering, School of Engineering, The University of Birmingham, Edgbaston, Birmingham B15 2TT, UK

ABSTRACT

Despite widespread use of the technique for a long time, the proper interpretation of mercury porosimetry data, particularly retraction curves, remains uncertain. In this work, the usefulness of two complementary techniques, mean-field density functional theory (MF-DFT) and micro-computerized X-ray tomography (micro-CXT), for aiding interpretation of ambiguous mercury porosimetry data has been explored. MF-DFT has been used to show that a specific, idiosyncratic form for the top of the mercury intrusion and extrusion curves is probably associated with a particular network structure where the smallest pores only form through connections between larger pores. CXT has been used to study the pore potential theory of hysteresis and entrapment directly using a model porous material with spatially varying pore wetting properties. CXT has also been used to directly study the percolation properties, and entrapment of mercury, within a macroporous pellet. Particular percolation pathways across the heart of the pellet have been directly mapped. The forms of entrapped mercury ganglia have been directly observed and related to retraction mechanisms. A combination of CXT and mercury porosimetry can be used to map spatial variation in pore neck sizes below the spatial resolution of imaging.

1. Introduction

Mercury porosimetry is probably still the only method by which a macroscopic porous material containing pores of potentially all sizes in the range ∼3 nm to ∼100 μm can be characterised using just a single technique. In principle, mercury porosimetry can be used to obtain the porosity, specific pore volume, pore connectivity (Portsmouth and Gladden, 1992), and the spatial distribution of pore size (Rigby, 2000). The method is based on the fact that mercury is non-wetting for most surfaces, and thus requires the imposition of an elevated pressure to penetrate a porous solid. The basic experiment consists of incrementing the pressure by a small step, allowing the system to reach equilibrium, and then measuring the volume of mercury that has entered the sample during that pressure step. This process is generally repeated until the maximum pressure possible with the apparatus used is obtained. The pressure can then be decremented in small steps back to ambient. However, in addition, more complex experiments can be performed using scanning

loops (Rigby et al., 2002) or mini-loops (Portsmouth and Gladden, 1992) to obtain more detailed void space descriptors.

The raw data obtained via the standard experiment, consisting of curves of volume intruded against imposed pressure, are typically converted into a volume-weighted, pore diameter distribution using the Washburn (1921) equation. The general relation for the pressure of mercury to fill a pore of a particular radius, r, is

$$p_f^l = \frac{-2\gamma \cos\theta}{r} \tag{1}$$

where p_f^l is the hydrostatic pressure in the liquid phase, γ is the surface tension and θ is the contact angle. This equation was derived for long cylindrical pores and its use requires the assumption that the surface tension and contact angle are not functions of pore size, or, for chemically heterogeneous systems, surface chemistry. A typical feature of mercury porosimetry data is a hysteresis between the intrusion and extrusion curves. Mercury tends to leave a sample at a much lower pressure than it originally entered. Several different theories have been suggested to account for this phenomenon, including contact angle hysteresis (Van Brakel et al., 1981), a pore potential effect (Lowell and Shields, 1984), or the energy requirement to generate a free

meniscus on breaking the mercury ganglion at initiation of retraction (Giesche, 2006). In order to account for variations of surface tension and contact angle with pore size, and for contact angle hysteresis, Kloubek (1981) obtained correlations for the $\gamma \cos \theta$ term in the Washburn equation as a function of pore size, and whether mercury was intruding or retreating. These correlations were obtained from measurements of the pressure required to intrude or extrude mercury from model controlled pore glass (CPG) materials which had different, but very narrow, pore size distributions that had been measured independently using electron microscopy (Liabastre and Orr, 1978). More recently (Rigby, 2002), analogous correlations have been obtained for alumina materials, and have been found to be independently predictive using integrated gas sorption experiments (Rigby and Fletcher, 2004).

The calibrated versions of the Washburn equation are only suitable for chemically homogeneous materials similar to the original model materials, such as sol–gel silica (Rigby and Edler, 2002) and alumina (Rigby, 2002) catalyst support pellets. However, it has also been shown (Rigby and Chigada, 2010) that the calibrated equations do not work for materials with significantly different levels of small-scale surface roughness to the original model materials. In addition, Milburn et al. (1994) have shown that the addition of metal crystallites to the surface of alumina catalyst supports leads to significant changes to the mercury porosimetry curves. Lowell and Shields (1982) found that the addition of metal salts to the surface of aluminas led to changes in the shapes of the intrusion and extrusion curves, and increased entrapment levels. Thommes et al. (2008) compared mercury porosimetry data for native silica monoliths with that for monoliths that had n-alkyl groups grafted to the surface. This led to changes in intrusion pressures and pore volumes, but made little difference to entrapment. These workers attributed variations in entrapment levels in different materials to differences in mass transfer properties.

Even once the surface geometry and chemistry issues involved in the conversion of the raw intrusion data to the pore size distribution have been addressed, the data so-obtained is only one-dimensional, and thus does not contain any information on the spatial distribution of pore size. This means that mercury is thus prone to the pore 'shadowing' or 'shielding' effect. Since mercury enters pores in order of decreasing size only as the pressure is increased, then a larger pore externally accessible only via a smaller pore will be perceived as a volume of smaller pores. As porosimetry is an indirect method, a model of interpretation representing the porous structure is required to obtain a de-shielded pore size distribution corrected for this effect, or to derive pore connectivity and other parameters. Previous structural models have included pore bond networks (Androutsopoulos and Mann, 1979), combined pore body and neck networks (Matthews et al., 1995), and packings of spheres (Bryant et al., 1996). Despite the use of sophisticated experiments, such as mini-loops (Portsmouth and Gladden, 1992), to enrich the data obtainable from mercury porosimetry, the structural models obtained are still highly oversimplified representations of the real porous medium. However, this does mean that, unlike for the real void space, complex coupled diffusion and reaction problems are more mathematically tractable for the model system.

More recently, more direct three-dimensional reconstructions have been obtained of void spaces using imaging techniques such as computerised X-ray tomography (CXT) (Hyväluoma et al., 2004), magnetic resonance imaging (MRI) (Baldwin et al., 1996), dual beam scanning electron microscopy (Holzer et al., 2004) and electron tomography (Koster et al., 2000). However, these techniques have limitations in the lower length-scale limit for the possible resolution and/or the sample size that may be studied at

high-resolution. MRI can only directly image pore spaces down to $\sim 10\ \mu m$, and CXT, using a synchrotron source, can reach ~ 50–100 nm resolution. While electron tomography can image down to the order of a few nanometres in scale, it can only do so for samples with an overall size of a few hundred nanometres, which may not be statistically representative of a macroscopically heterogeneous material. There is thus a lack of a suitable technique to be able to obtain information on a pore system below the resolution of the imaging methods, such as CXT, but that is spatially resolved and statistically representative of the macroscopic sample as a whole. More positively, however, CXT has the advantage of being a non-destructive and non-contact inspection technique which is unlimited by the complexity of internal and external surfaces of the test material (Burch, 2002; Phillips and Lannutti, 1997).

CXT uses a combination of X-ray microscopy and tomographical algorithms which are based on the contrast in X-ray images generated by the differences in X-ray attenuation (absorption and scattering) arising from the differences within the specimen material density (Mousavi et al., 2005). The X-rays are passed through a specimen which is rotated in numerous directions to produce an image which displays differences in density at thousands of points in the 2D slices produced (Mousavi et al., 2005). Many contiguous slices are produced and these are stacked to produce a 3D reconstruction of the object; these are true cross-sectional images and accurately depict the component geometry up to a certain resolution (Burch, 2002). A schematic diagram of the XRCT principle is shown in Fig. 1.

In this work, it will be shown how a combination of mercury porosimetry with CXT can overcome the limitations of each to deliver a means to obtain the spatial arrangement and connectivity of small pore necks (below CXT resolution) that guard access to larger pore bodies. CXT will be used to test the pore potential model of mercury porosimetry hysteresis and entrapment in a study of mercury intrusion and retraction within a model system consisting of an 'eggshell' platinum–alumina catalyst. Finally, CXT will be utilised to visualise mercury-intruded tri-modal α-alumina sample pellets. The aim here is to explore the possibilities in assessing key porous network characteristics such as porosity, pore connectivity and pore network homogeneity via the complementary use of mercury porosimetry and CXT.

In addition to new experimental techniques to characterise porous structures, alternative means to the Washburn equation have also been developed to inform the interpretation of mercury porosimetry data, such as statistical mechanical methods using mean-field density functional theory (MF-DFT) (Porcheron and Monson, 2004; Porcheron et al., 2007). MF-DFT uses a lattice-based representation of the porous material and thus can cope with the high degree of complexity associated with real amorphous materials. It has been found that porosimetry phenomena, such as hysteresis, naturally emerge from these models. These
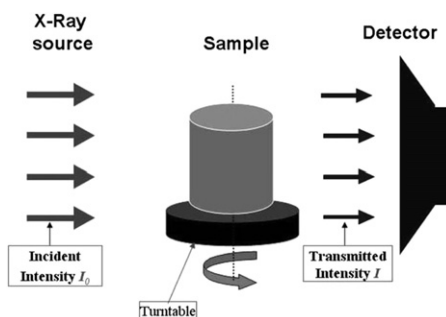

Fig. 1. A schematic diagram illustrating the basic principle of CXT (Miguélez-Morán et al., 2009).

models thus offer the possibility of being able to incorporate both the geometric and chemical heterogeneity associated with highly complex systems, such as supported metal catalysts. In this work, it will be shown that MF-DFT can be used to demonstrate that, using a combination of both mercury intrusion and extrusion data, information can be obtained on the connectivity of pores of different sizes simply from the basic mercury porosimetry experiment, without the need for the many implicit assumptions and additional experiments required with pore bond network models.

The overall aim of this paper is to demonstrate how novel uses of the complementary techniques of MF-DFT and CXT can improve the interpretation of raw mercury prosimetry data, thereby providing significant improvements, compared with previous approaches, to the pore structure information obtainable. The form of raw mercury porosimetry curves is affected by various different aspects of the structure of the porous material that arise over several different, and often widely disparate, length-scales, such as pore connectivity at the nanometre scale for mesoporous solids, and macroscopic variations in local average (meso)pore size over the micro- to millimetre length-scale, as seen in MRI studies (Rigby and Gladden, 1996). Hence, for real porous materials with structural features over many length-scales, a combination of different techniques appropriate to these different length-scales is required. MF-DFT will be used to consider pore-scale aspects, while CXT will be used to look at larger length-scale aspects. Hence, this paper is structured as follows. First, this paper will show how MF-DFT can be used to interpret particular idiosyncratic features of the mercury porosimetry data for some types of samples to obtain information on the pore connectivity. Second, this paper will show how CXT can be used to directly study the pore potential theory of mercury porosimetry hysteresis and entrapment, and to obtain more direct evidence for this theory compared to previous approaches. Third, this paper will show how CXT can be used to study the percolation pathways and conformations of entrapped mercury ganglia in certain macroporous materials

2. Theory

2.1. Mercury porosimetry

In general, raw data from mercury porosimetry is analysed using the Washburn (1921) equation. However, it is well known (Van Brakel et al., 1981) that both the surface tension γ and contact angle θ vary with the radius of curvature of the meniscus, and that the contact angle depends upon whether the meniscus is advancing or receding. More recently (Kloubek, 1981; Rigby, 2002), correlations for the product $\gamma \cos \theta$ have been introduced that take into account these effects. These correlations have been derived by calibrating the pressure p at which mercury enters or leaves a model porous medium with a regular structure against an independent measure of pore size r, such as electron microscopy (Liabastre and Orr, 1978). Insertion of these correlations into the Washburn equation gives rise to expressions of the form

$$r = \frac{-A + \sqrt{(A^2 - 2pB)}}{p} \qquad (2)$$

where A and B are constants depending on the material, and whether the mercury meniscus is advancing or retreating. The values of A and B for silica and alumina are given in Table 1. The expressions of the form of Eq. (1) are empirical in origin, and are, therefore, of limited range of applicability (see Table 1), and also contain experimental error ($\sim$4–5% (Kloubek, 1981). However, more recent work (Rigby and Chigada, 2010), using MF-DFT, has now elucidated why the calibrated Washburn equations work as

Table 1
Parameters for use in Eq. (2).

Material	$A.10^3/$ (N m^{-1})	$B.10^{12}$/N	Range of validity/(nm)
Silica (advancing meniscus)	− 302.533	− 0.739	6–99.75
Silica (retreating meniscus)	− 68.366	− 235.561	4–68.5
Alumina (advancing meniscus)	− 302.533	− 0.739	6–99.75
Alumina (retreating meniscus)	− 40	− 240	4–68.5

they do, removing apparent 'contact angle hysteresis' effects, and thus the equations need no longer be considered simply as 'phenomenological' since a firmer understanding of the processes underlying mercury porosimetry hysteresis has now been obtained. This previous work has demonstrated that the width of single pore hysteresis is linked to the degree of surface roughness which affects the multiplicity of metastable states possible for the fluid. Those materials, including those considered below, for which the calibrated Washburn equations can achieve superposition of the raw intrusion and extrusion curves share similar levels of surface roughness to the model materials used to originally obtain the equations.

2.2. Lattice-based, mean-field (density functional) theory (MF(DF)T)

In MF-DFT, for a single occupancy lattice gas with nearest neighbour interactions, the grand potential, Ω, associated with the lattice gas Hamiltonian can be written (Porcheron et al., 2007) as

$$\beta\Omega[\zeta_i] = \sum_i [\rho_i \ln \rho_i + (\zeta_i - \rho_i)\ln(\zeta_i - \rho_i) - \beta\mu\rho_i] - \beta\varepsilon_{ff}$$
$$\sum_{<ij>} [\rho_i\rho_j + \alpha\rho_i(1-\zeta_j) + \alpha\rho_j(1-\zeta_i)], \qquad (3)$$

where $1/kT$ is denoted β, ρ_i is the local density at site i, k is the Boltzmann's constant, T is the absolute temperature, μ is the chemical potential, ε_{ff} is the strength of nearest neighbour interaction and α is the ratio of the wall–fluid to the fluid–fluid interaction parameter. Each site could either be occupied by a solid particle ($\zeta = 0$), or be available for fluid occupation ($\zeta = 1$). The necessary condition for an equilibrium state (a minimum in Ω) is that the partial derivative of Ω with respect to local density at each site vanishes. Applying this condition to Eq. (3) and rearranging yields the following set of nonlinear algebraic equations that can be solved iteratively to yield the density distribution at a given value of μ and T

$$\rho_i = \frac{\zeta_i}{1 + \exp\left[-\beta\mu - \beta\varepsilon_{ff}\sum_{j \in i}[\rho_j + \alpha(1-\zeta_j)]\right]}, \qquad (4)$$

where the summation over j is taken over the nearest neighbours of site i. The set of equations is solved by iteration with a convergence criterion such that the differences in individual values of ρ_i from successive iterative rounds are within $\sim 10^{-9}$ of the previous value.

Mercury porosimetry intrusion and extrusion curves can be obtained by gradually incrementing the chemical potential, from a value well below the intrusion value, in small steps ($\Delta(\beta\mu) = (\frac{5}{3}) \times 10^{-3}$) to mimic the process in the real experiment. At the start, the adsorbate densities within the pore itself were set to a small value below that encountered in the intrusion curve to mimic the initial near-vacuum state in experiments, and subsequently each initial guess for the set of densities at each isotherm point was taken as the solution set for the last isotherm point. To simulate the initial immersion of the sample in the mercury bath during porosimetry the starting guesses for the density in the bulk reservoirs at either end of the pore were initially set to unity.

Retraction curves were obtained in a similar manner by decreasing the chemical potential for each step. Previous work (Rigby and Chigada, 2010) has shown that the density profiles obtained are independent of solution method and, thus, the algorithm used by Libby and Monson (2004), consisting of using only the values of ρ_i obtained in the 'previous round' of the iteration in Eq. (4) for the current round, will be used.

For a lattice gas model, the chemical potential at saturation is known analytically, and is given by $\mu_0 = -Z\varepsilon_{ff}/2$ (and thus for the simple cubic lattice used in this work, $\mu_0 = -3\varepsilon_{ff}$) (Libby and Monson, 2004). The simulated isotherms obtained could thus be presented as density against relative activity, λ/λ_0, where $\lambda = exp(\mu/kT)$, as well as against chemical potential. For a lattice gas on a simple cubic lattice, $kT_c/\varepsilon_{ff} = 3/2$. For typical experimental conditions in mercury porosimetry, $T/T_c = 0.17$ (Porcheron et al., 2007).

2.2.1. Pore models

The pore models for the studies of pore connectivity were generated on a lattice of overall dimensions of $70 \times 70 \times 130$ sites. The porous solid occupied a region of $70 \times 70 \times 80$ sites in the middle of the longest side of the lattice. The basic model consisted of two large cuboid pores of dimensions $20 \times 20 \times 80$ sites arranged with their longest sides parallel to each other and the longest side of the overall lattice, as shown in Fig. 2. At each entrance to the large pores a bulk reservoir of size $70 \times 70 \times 25$ sites was located. Periodic boundary conditions applied at the edges of the bulk reservoir regions. Two smaller pores, of size $3 \times 3 \times 20$ sites, that bridged between the two larger pores were each located along the midline of the longest side of the large pores, at a distance of 25 lattice sites from the large pore mouths, as shown in Fig. 2. Most of the pore connectivity models used were variants of the above basic model, referred to as Model I. Model II was the same as Model I except that the large pores were now each of length of 79 sites, such that each large pore had a dead end at the same end as each other. Model III was the same as Model II, except that the smaller bridging pores each were of length 19 sites such that they had a dead end at opposite ends to each other. Hence, Model III consisted of two separated dead-end larger pores, each with a single dead-end side branch. Model IV consisted of a lattice with two separate dead-end, cuboid pores of size $3 \times 3 \times 79$ sites. Model V consisted of a lattice with two separate dead-end, cuboid pores of size $20 \times 20 \times 79$ sites. Models IV and V are considered to represent the key aspects of the pore systems in the CPGs used to obtain the parameters in Table 1. The CPGs have virtually uniform pore size and are likely to contain some dead-end pores.
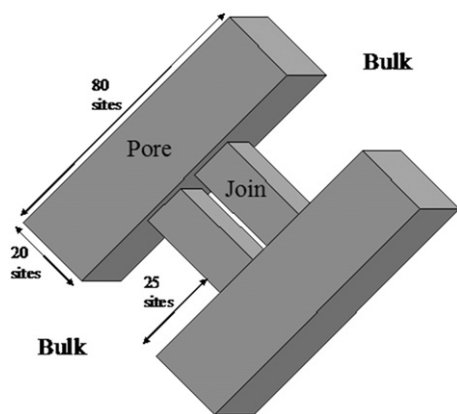

Fig. 2. A schematic diagram of the pore network Model I used in MF-DFT simulations.

2.2.2. X-ray computed tomography

X-ray computed tomography measures the transmitted intensity of a finely collimated beam of radiation (Phillips and Lannutti, 1997). A linear imaging device allows detection of the transmitted intensities along this beam, which is related to the integral attenuation of the materials encountered inside the scanned object (Douarche et al., 2001). For each sensitive pixel within the detector, the intensity is given by the Beer–Lambert law of absorption which states that each layer of material of equal thickness will absorb an equal fraction of the radiation which traverses it (de Paiva et al., 1998; Phillips and Lannutti, 1997) such that

$$\frac{I}{I_0} = exp\left(-\int_{x_0}^{x_1} \mu_a(x)dx\right) \tag{5}$$

where I_0 is unattenuated X-ray beam intensity, I is the intensity of the beam after it has traversed a layer of material of thickness x and $\mu_a(x)$ is attenuation coefficient as a function of x along the X-ray beam. Many measurements over many views are collected in XRCT resulting in a map of individual linear attenuation coefficients within the studied cross section (Phillips and Lannutti, 1997).

Each linear attenuation coefficient, μ_a, is dependent on both the mass attenuation coefficient and mass density. Also, as an X-ray beam passes through a material, given its polychromatic nature, lower energies are preferentially absorbed as μ_a is energy dependent (Lin and Miller, 2001). Furthermore, individual material heterogeneities, and the use of different materials within a system, affects the ultimate value of μ_a (Miguélez-Morán et al., 2009). Hence, an overall approximate relationship for μ_a is given as (McCullough, 1975)

$$\mu_a = \rho \frac{Z}{A} N_{AV}\left(a + b\frac{Z^{3.8}}{E^{3.2}}\right) \tag{6}$$

where ρ is the material density, Z is the effective atomic number, A is the effective atomic weight, N_{AV} is the Avogadro's number, a and b are the material constants and E is the photon energy.

3. Experimental

The samples studied in this work included commercially available silica and alumina blank catalyst support materials. Samples G2, S1 and SG1 were sol–gel silica spheres. Sample E1 consisted of cylindrical alumina tablets, each with diameter and height both equal to ~3 mm. Samples SG2, SG3 and SG4 each consisted of a spherical α-alumina pellet with typical diameter of ~4–5 mm and a nitrogen BET surface area of ~0.75 m²/g. Also studied was a platinum (0.5% Pt) egg-shell catalyst supported upon a cylindrical alumina tablet with diameter and height both equal to ~3 mm. The catalyst has a BET surface area of 109 m²/g and a Pt dispersion of 26.8%.

3.1. Mercury porosimetry

Mercury porosimetry experiments were performed, using a Micromeritics Autopore IV 9420, on all samples. The sample was first evacuated to a pressure of 6.7 Pa in order to remove physisorbed gases from the interior of the sample. Porosimetry experiments were conducted with an equilibration time of 15 s. All of the samples studied in this work retained structural integrity during porosimetry. For each sample run the pressure was increased incrementally from an evacuated pressure and then pressure was decreased incrementally back to atmospheric.

3.2. Computerised X-ray tomography

3.2.1. Scanning and reconstruction

Pellets were scanned using a high resolution Skyscan 1072 desktop micro-CT system, which consists of a microfocus sealed X-ray tube with a spot size of 5 μm. The X-ray detector consisted of a 1024 × 1024 pixel 12-bit digital cooled CCD camera connected to a computer. For every pellet tested, the system was set at a voltage of 101 kV and a current of 98 μA. Before scanning could take place, the X-rays were aged over a period of 15 min to the operational settings; this procedure only needed to be carried out when the system was initially turned on.

X-rays were passed though the object material which is itself rotated inside the X-ray chamber so it can be viewed at different angles. A computer records each of the projected images and measures the intensity of the X-ray beam as it passes through the object material. Care was taken during the experimental setup to align the incumbent pellet correctly; it is imperative that the entire pellet width was included throughout the camera rotational view. Failure to do so would result in distortion in the images produced.

X-ray images were acquired from 200 rotational views through 180° of rotation (0.9° increments). CXT utilises polychromatic X-ray beams and low energy beams can be readily attenuated which can result in ring artefacts and beam hardening. A 1 mm aluminium filter was used to scan mercury intruded samples in order to reduce the above artefact which can heavily affect metals.

Image reconstruction was carried out using NRecon (ver. 1.5.1.4). The reconstruction algorithm is based on a filtered back projection procedure for fan-beam geometry with specific noise reduction corrections (Skyscan, 2003). The reconstruction of each of the 200 projections takes approximately 20 s per slice and produces a set of 1000 greyscale images which form an image stack with spacing in accordance to the system pixel size.

3.2.2. Image analysis methods

Image analysis of the reconstructed images was carried out using CT analyser (CT-An) (ver. 1.8.1.2) which allows 2D and 3D analysis of images. Data Viewer (ver. 1.3.2.1) was also used.

4. Results

4.1. Mercury porosimetry

Fig. 3 shows the mercury porosimetry data for a whole pellet sample and a fragmented sample from batch S1 that have been obtained previously (Rigby and Edler, 2002), and has been analysed using Eq. (2). It can be seen that, for the whole pellet, at larger pore sizes structural hysteresis, giving rise to entrapment, occurs, but at smaller pore sizes Eq. (2) achieves a complete superposition of the intrusion and extrusion curves. This finding is typical of findings for most mesoporous silica and alumina catalyst support pellets (Rigby and Edler, 2002). The top of the intrusion curve is the same shape for both whole and fragmented samples indicating no residual shielding at smaller pore sizes.

Figs. 4–6 show the mercury porosimetry data, analysed using Eq. (2), for whole pellet samples from batches G2, SG1 and E1. It can be seen that, within experimental error, Eq. (2) achieves a superposition of the intrusion and extrusion curves in the region associated with the modal pore size. However, it can also be seen that, for all three materials, superposition of the retraction curve, on top of the intrusion curve, is not obtained at the top of the main ascending/descending section. While the tops of the intrusion curves have a rounded knee, the tops of the extrusion curves
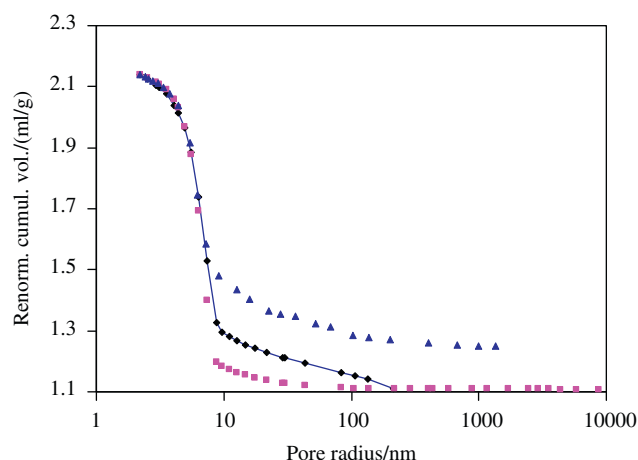

Fig. 3. Mercury porosimetry intrusion (■) and extrusion (▲) curves for a whole pellet sample, and the intrusion curve for a fragmented sample (◆), from batch S1 analysed using Eq. (2) and the appropriate parameters from Table 1.
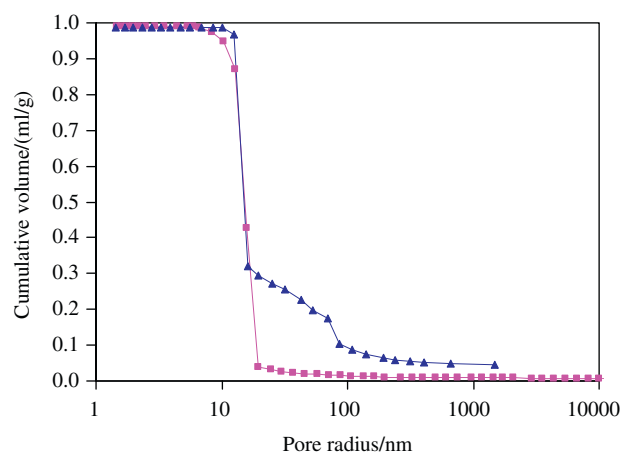

Fig. 4. Mercury porosimetry intrusion (■) and extrusion (▲) curves for a whole pellet sample from batch G2 analysed using Eq. (2) and the appropriate parameters from Table 1.

Fig. 5. Mercury porosimetry intrusion (■) and extrusion (▲) curves for a whole pellet sample from batch SG1 analysed using Eq. (2) and the appropriate parameters from Table 1.

exhibit a much sharper knee, such that some hysteresis between the two curves is retained. Previous work (Rigby et al., 2008) has demonstrated that the particular idiosyncratic form associated

Fig. 6. Mercury porosimetry intrusion (■) and extrusion (▲) curves for a whole pellet sample from batch E1 analysed using Eq. (2) and the appropriate parameters from Table 1.
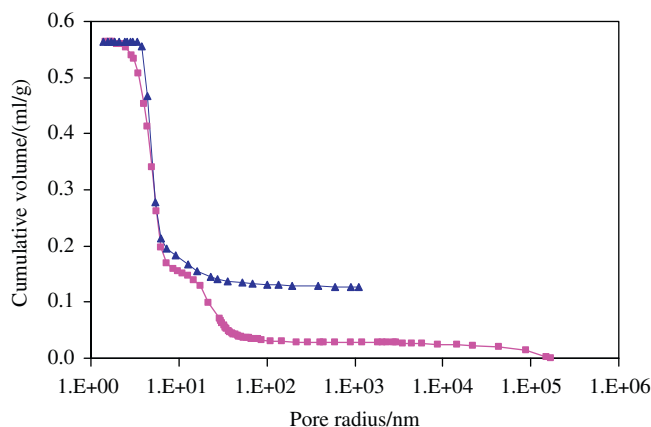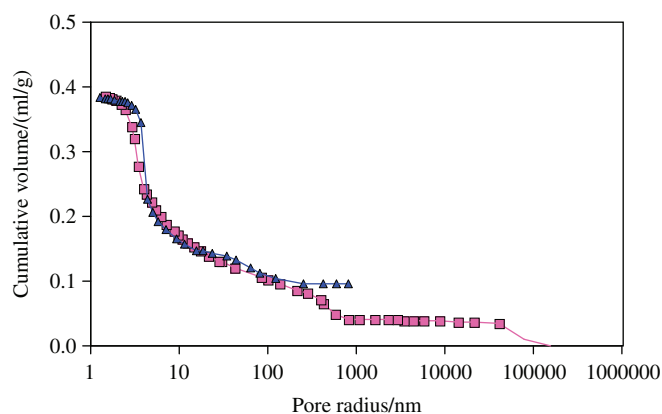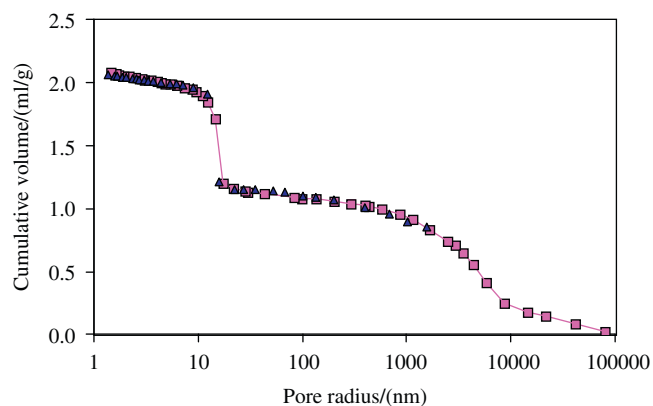

Fig. 7. Mercury porosimetry intrusion (■) and extrusion (▲) curves for a fragmented sample from batch G2 analysed using Eq. (2) and the appropriate parameters from Table 1.

Fig. 8. Mercury porosimetry intrusion (■) and extrusion (▲) curves for a fragmented sample from batch E1 analysed using Eq. (2) and the appropriate parameters from Table 1.

Fig. 9. Mercury porosimetry intrusion (■) and extrusion (▲) curves for a whole pellet sample of the Pt/alumina catalyst pellets analysed using Eq. (2) and the parameters for alumina from Table 1.

Fig. 10. Example of the simulated intrusion and extrusion curves for the main pore (solid line) and join (dashed line) elements of network Model I obtained using MF-DFT.

with the retraction knee for materials such as G2, under study in this work, is independent of pressure step equilibration time in the porosimetry experiment, and thus is not due to dynamic effects.

Figs. 7 and 8 show the mercury porosimetry data for fragmented samples from batches G2 and E1. It can be seen that, while sample E1 retains the hysteresis at the top of the porosimetry curves following fragmentation, for batch G2 there is some evidence of a rounding of the top of the extrusion curve such that the amount of hysteresis is significantly reduced.

These findings suggest that for some materials, such as S1, smaller pores fill in sequence with increasing pressure and then empty in a simple reversal of the intrusion process, as the pressure is decreased. However, the results for other materials, such as G2, SG1 and E1, suggest that while pore filling occurs in a similar manner to S1, the extrusion process is very different. For this second class of materials, extrusion of the smallest pores is delayed until the pressure, as given by Eq. (2), required for extrusion of larger pores is obtained and then all pores smaller than this size empty at once.

Fig. 9 shows the mercury porosimetry data for the platinum/alumina catalyst analysed using Eq. (2) and the parameters for alumina given in Table 1. It can be seen that the retraction curve becomes superposed on the intrusion curve at small and intermediate pore sizes until entrapment begins in larger mesopores and the macropores.
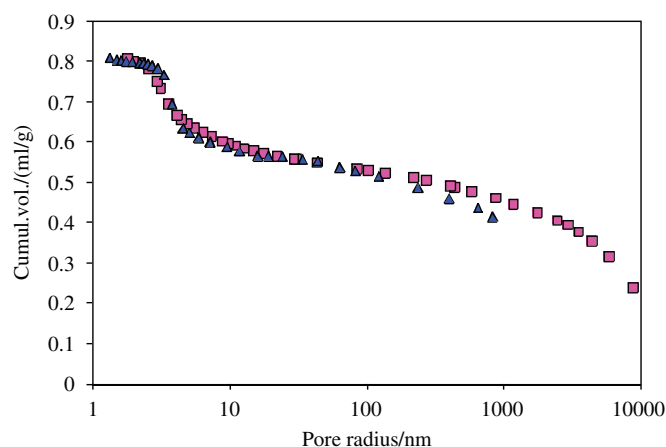
4.2. Lattice-based, mean-field (density functional) theory

Examples of the simulated intrusion curves for the main pores and the connecting joins for Model I are shown in Fig. 10. Similar

Table 2
Chemical potentials for intrusion and extrusion from model elements determined from MF-DFT simulations.

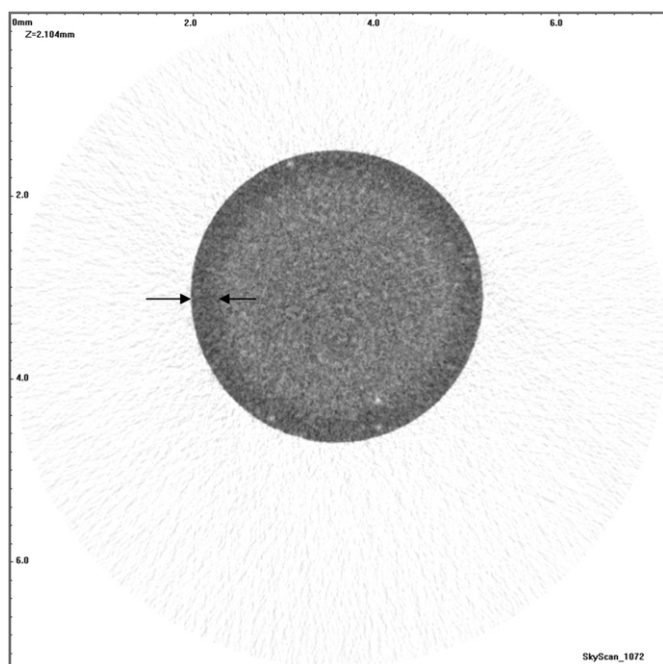| Model	Element	Intrusion chemical potential, $\beta\mu$	Extrusion chemical potential, $\beta\mu$
I	$20 \times 20 \times 80$ through pore	-7.60500	-13.12000
	$3 \times 3 \times 20$ joins	-7.43500	-13.11500
II	$20 \times 20 \times 79$ dead-end pore	-7.60500	-11.83000
	$3 \times 3 \times 20$ joins	-7.43500	-11.83000
III	$20 \times 20 \times 79$ dead-end pore	-7.60500	-11.83000
	$3 \times 3 \times 19$ dead-end side arm	-7.43167	-10.95000
IV	$3 \times 3 \times 79$ dead-end pore	-7.43167	-10.95000
V	$20 \times 20 \times 79$ dead-end pore	-7.60500	-11.83000

Fig. 11. Two-dimensional, radial cross-section through three-dimensional reconstructed CXT images of the platinum/alumina catalyst. The arrows indicate the position of the higher X-ray adsorption due to the Pt egg-shell layer.

data were also obtained for Models II–IV. The chemical potentials for the modal intrusion and extrusion steps in/out of the main elements of the pore models are shown in Table 2. From Table 2 it can be seen that, for model networks (Model III) that consist of smaller dead-end pores leading off larger dead-end pores, the filling and emptying with mercury proceeds in a similar fashion to the individual pore Models (IV and V) that represent the CPGs originally used to obtain the parameters in Eq. (2). However, for the Model (II) with dead-end larger pores and through smaller connections, the pore elements fill in order of decreasing size as chemical potential (pressure) is increased, but empty together at the chemical potential expected for the larger dead-end pores. This is the same type of behaviour as for the real materials E1, G1 and SG1. For the Model (I) with both through main pores and through joins retraction is considerably delayed in both sets of pore elements and occurs at slightly different chemical potentials (pressures).

4.3. CXT of samples containing entrapped mercury

4.3.1. Platinum–alumina egg-shell catalyst

Fig. 11 shows a two-dimensional, radial cross-section through a three-dimensional reconstructed CXT image of the fresh platinum/alumina catalyst. From a comparison of the variation in pixel intensity across the image of the Pt/alumina eggshell catalyst, it

can be seen that the egg-shell layer of platinum near the surface of the catalyst tablet shows up as a darkened annulus around the edge of the image. This is probably due to the increased absorption of X-rays that occurs in the region containing platinum due to its higher electron density compared to the surrounding alumina support.

Fig. 12(a) shows a two-dimensional, radial cross-section through a three-dimensional reconstructed CXT image of the platinum/alumina catalyst following a mercury porosimetry experiment where the mercury pressure was increased up to 414 MPa and then back to ambient. Fig. 12(b) shows an axial cross-section of the same pellet, following mercury porosimetry, supported on top of a fresh catalyst pellet. From these figures it can be seen that absorption of X-rays has increased even further in the annular ring at the periphery of the pellet, compared to absorption in the fresh catalyst. Small areas of increased X-ray entrapment are also observed sporadically across the central region of the pellet within the cross-section. The series of CXT images suggest that mercury predominantly becomes entrapped in those regions of the pellet pore space containing platinum metal. Fig. 13 shows a comparison of two-dimensional, radial cross-sections through three-dimensional reconstructed CXT images of a platinum/alumina catalyst pellet following a mercury porosimetry experiment both whole and following splitting in half with a scalpel. It can be seen that increased X-ray adsorption does not occur along the diameter along which the pellet was fractured. This indicates that the increased pixel intensity in the annulus around the periphery of the whole pellet is not an artefact of image reconstruction and processing.

4.3.2. α-alumina

In this section, sample SG2 represents a sample of the α-alumina pellet material intruded up to 2 bar ultimate pressure during mercury porosimetry; while SG3 is an α-alumina pellet sample that was intruded up to 5 bar, and SG4 is an α-alumina pellet sample that was intruded up to 10 bar. Fig. 14 shows the raw mercury porosimetry data, and the differential PSDs obtained from the raw data using the Washburn equation. Fig. 14 shows that smallest pore size probed (according to the Washburn equation) at 2 bar was 6.96 μm, at 5 bar was 2.96 μm, and at 10 bar was 1.47 μm. All pores probed up to 2 bar pressure are within the image resolution for CXT, and, thus, true mercury levels should be completely visible. For the 5 and 10 bar experiments, some sub-resolution mercury entrapment would be expected. From the raw data it can be seen that virtually all of the mercury is entrapped in the sample at the end of the experiments.

Reconstructed images of samples SG2, SG3 and SG4 were visualised using CT-An. Reconstructed images were originally produced as a transaxial image stack, but could be re-sliced in the coronal and sagittal directions using Data Viewer. Reconstructed CXT images, such as Fig. 15a, exhibited streak artefacts, making further analysis difficult. However, it was possible to use
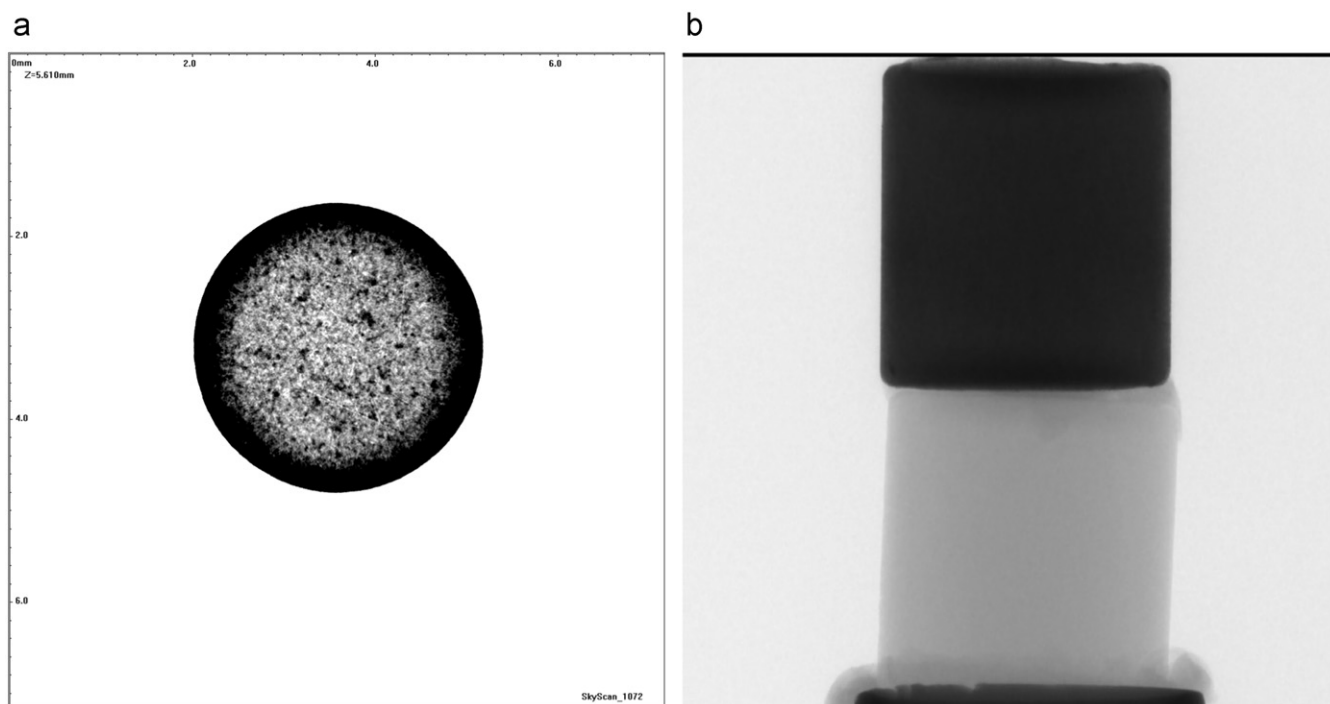
Fig. 12. (a) A two-dimensional, radial cross-section through a three-dimensional reconstructed CXT image of the platinum/alumina catalyst following a mercury porosimetry experiment where the mercury pressure was increased up to 414 MPa and then back to ambient and (b) an axial cross-section of the same pellet, following mercury porosimetry, supported on top of a fresh catalyst pellet.
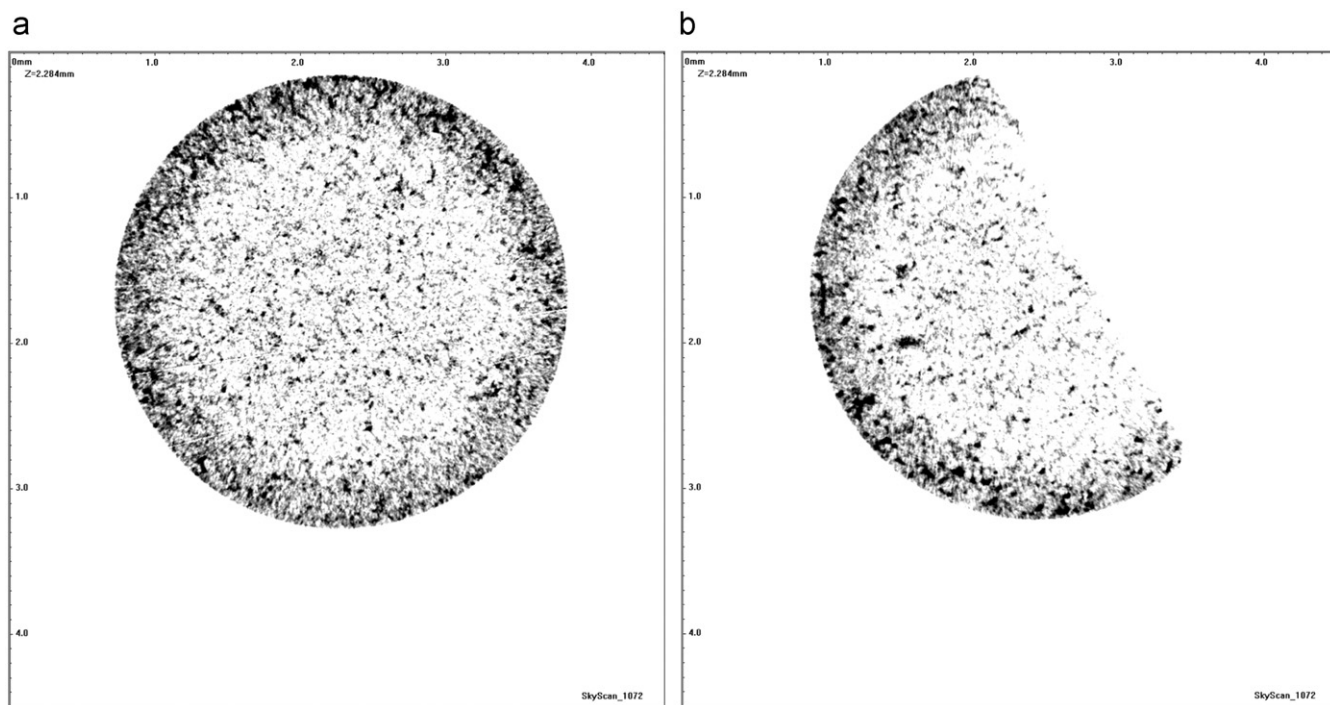

Fig. 13. A comparison of two-dimensional, radial cross-sections through three-dimensional reconstructed CXT images of a platinum/alumina catalyst pellet following a mercury porosimetry experiment both whole (a) and following splitting in half with a scalpel (b).

Data Viewer to provide improved clarity by re-slicing the image stacks in the coronal and sagittal direction, as found previously in the literature (Reimann et al., 1997).

Fig. 15b shows an example of an image slice of sample SG2 in the coronal direction. The visible pore regions represent those filled with denser mercury material. In Fig. 15b, high mercury coverage can be seen around the pellet periphery. There are also clear bands of entrapped mercury that cross the interior of the pellet that are surrounded by regions containing little, or no, entrapped mercury. Since, for the lowest ultimate pressure intrusion virtually all of the mercury intruded became entrapped, this finding suggests there are only a limited number of available
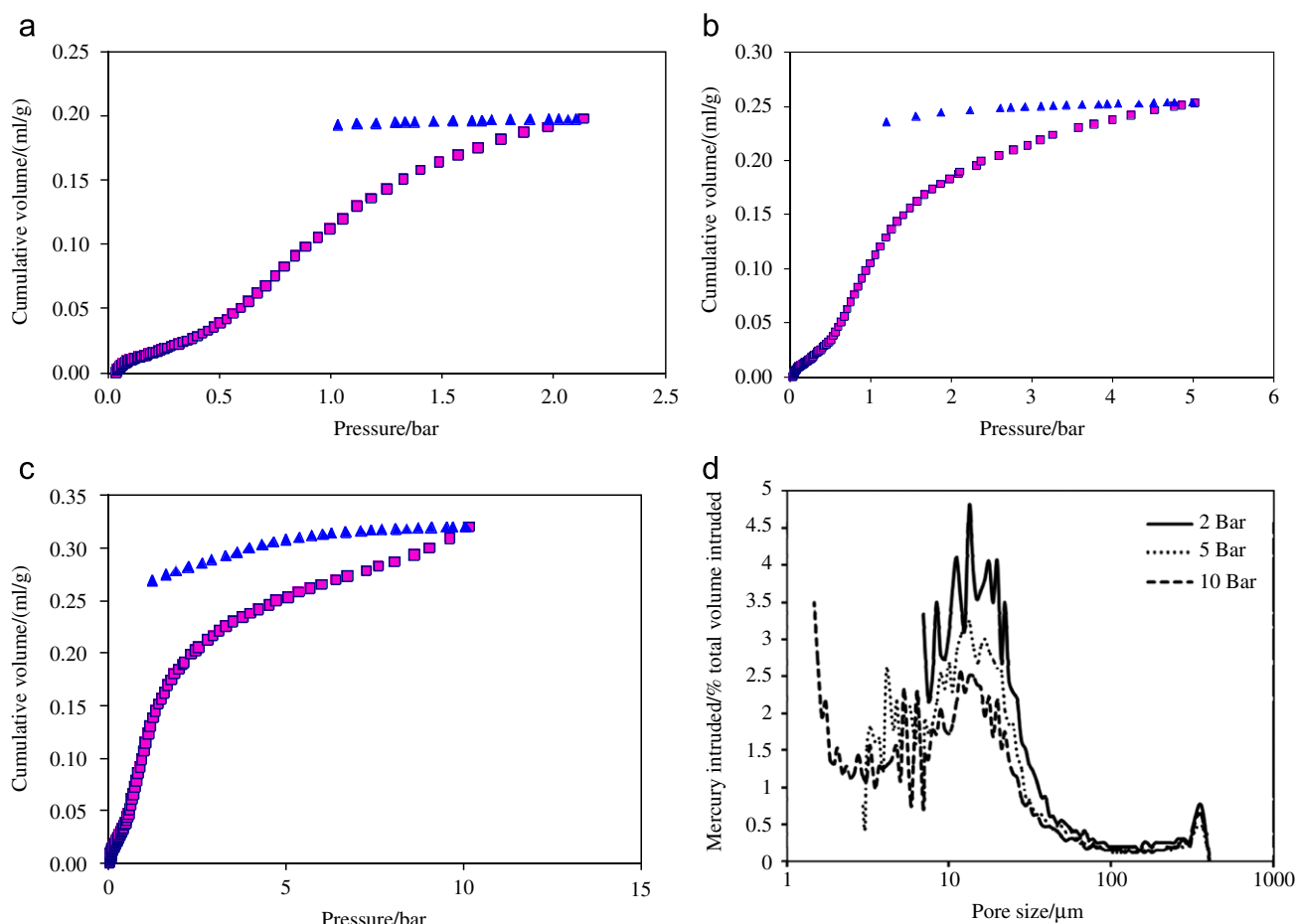
Fig. 14. Raw mercury intrusion (■) and extrusion (▲) scanning curves for samples SG2 (a), SG3 (b) and SG4 (c) and (d) incremental pore size distributions for the α-alumina pellets obtained from mercury porosimetry experiments intruded up to various different ultimate intrusion pressures.

percolation routes across the centre of the pellet for mercury intrusion at 2 bar maximum pressure.

Fig. 15c and d show that increasing mercury intrusion pressure results in a different entrapment profile. While individual pores filled with mercury are clearly visible at the pellet periphery, towards the centre of the pellet there appears to be many areas of 'apparent' mercury coverage with greyscale values in between those of actual mercury and α-alumina material. This may represent mercury filled pores which are smaller than the image resolution. Individual mercury-filled pores at the centre, however, are seldom seen. The vast majority of clearly visible mercury-intruded pores are seen to be greater than 50 μm in diameter for all experiments. Several more detailed images and their descriptions are given in Appendix A.

Porosity distributions within the pellets, for pores above a certain size, can be derived, quantitatively, by investigating mercury entrapment as a function of pellet radius, as shown in Fig. 16. To obtain Fig. 16, 3D analysis in CT-An was performed by selecting individual annular volumes of the pellets tested. As annular volumes were taken during this process, an implicit assumption was made that the pellets were spherical. Although this assumption does not fully reflect the true shapes of the pellets (which exhibit a degree of deviation from a spherical shape) the method is the most pragmatic approach. In order to assess the distribution of mercury entrapment by this method, an understanding of the nature of mercury attenuation is required. In Fig. 16, attenuation values plotted in the grey value range 150–255 were selected, to reflect the dense and strongly attenuating nature of mercury. From Fig. 16, it can be seen that,

following intrusion up to 2 bar, the spatial distribution of entrapped mercury, and thus pores accessible by necks of sizes above 6.96 μm, is not homogeneous.

5. Discussion

5.1. Lattice-based, mean-field (density functional) theory

The findings from the MF-DFT simulations on model pore networks suggest that materials where Eq. (2) can be used to obtain a complete superposition of raw intrusion and retraction curves at smaller pore sizes consist of pore systems with relatively low connectivity between the smallest pores and slightly larger pores. However, when the smallest pores are co-ordinated to more slightly larger pores, such that they form a through network, this results in a delay in mercury retraction from these pores, and the local area pore network all empties together. These findings suggest that, for materials such as E1, G2 and SG1, pores of the size equal to that corresponding to the sharp knee in the retraction curve have direct access to the exterior, and are interconnected by the smaller pore sizes intruded in the top section above them in the cumulative intrusion curve.

Similar stretched 's'-shaped intrusion and right-angled extrusion curves, to those shown above for mercury porosimetry for E1, G2 and SG1, have been found for water porosimetry of partially wetting carbon/polymer gas diffusion layer materials (Gostick et al., 2009). This suggests that the phenomena described
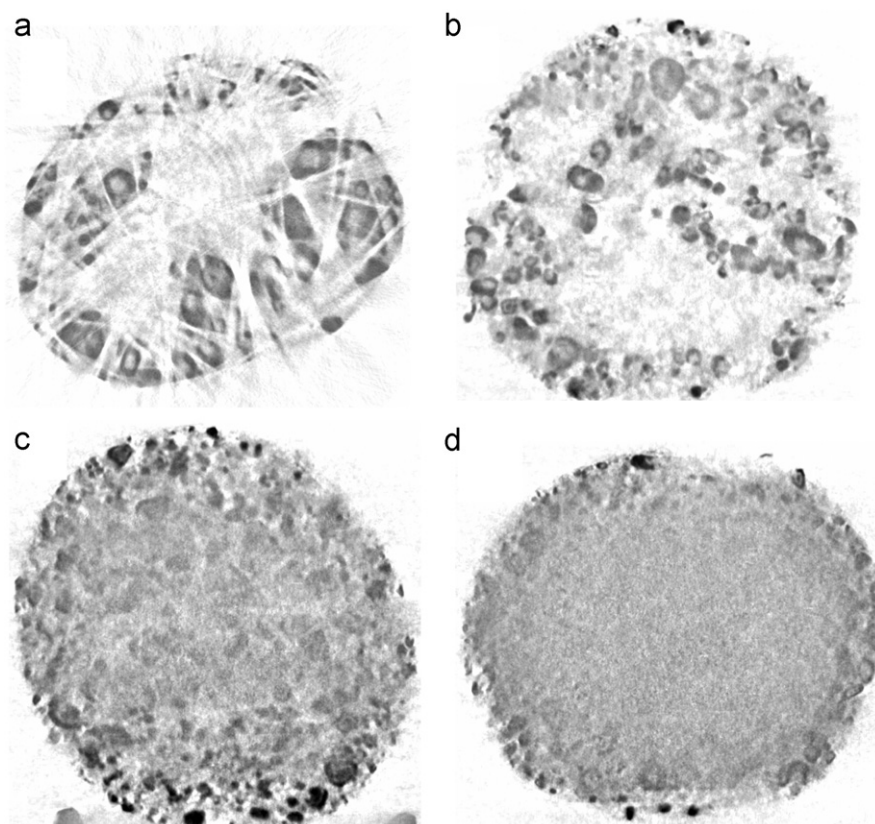
Fig. 15. Reconstructed greyscale image slice of α-alumina pellets: (a) sample SG2 in the transaxial direction and (b–d) samples SG2, SG3 and SG4, respectively, in the coronal direction.
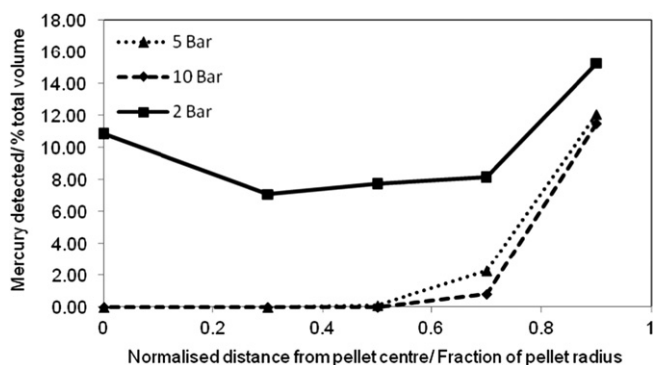

Fig. 16. Variation of apparent mercury entrapment in α-alumina pellets plotted against a normalised distance from the pellet centre.

above may apply more widely to liquid porosimetry of non-wetting fluids in general.

5.2. CXT of samples containing entrapped mercury

5.2.1. Platinum–alumina egg-shell catalyst

It has been found above that mercury entrapment within a platinum/alumina eggshell catalyst predominantly arises in the regions of the void space containing platinum metal. A consideration of intermolecular forces (Zhu, 1995) suggests that mercury will wet platinum. Hence, pores in those regions of the pellet containing platinum are likely to be more wetting of mercury than purely alumina pores. Therefore, it seems likely that the increased pore potential caused by the presence of platinum leads to the mercury entrapment. The presence of platinum crystallites is also likely to lead to a roughening of the pore surface. However,

previous MF-DFT simulation and experimental work (Rigby and Chigada, 2010) has suggested that a simple roughening of pore walls leads to a narrowing of mercury porosimetry hysteresis because the increased numbers of potential metastable states resulting from the roughened walls facilitates retraction. The findings from CXT studies reported here are consistent with the more indirect studies conducted by Milburn et al. (1994), who showed that the addition of metal crystallites to the surface of alumina catalyst supports lead to significant changes to the mercury porosimetry curves. However, this previous work did not provide evidence that the changes in the mercury porosimetry curves resulted from the presence of the metal rather than some modification to the rest of the surface during the deposition of the metal.

5.2.2. α-alumina

5.2.2.1. Random and non-random heterogeneities. The results shown above suggest there is a high degree of heterogeneity within the α-alumina pore network giving rise to mercury entrapment. While Fig. 15b shows large regions where no mercury was entrapped, suggesting that the larger pores probed during the 2 bar mercury porosimetry do not pervade the whole pellet, for the pellets resulting from the 5 and 10 bar mercury porosimetry tests, depicted in Fig. 15c and d, there was a more homogenous occurrence of entrapped mercury across the pellets. This suggests a more even spatial distribution of the pore sizes probed up to 5 and 10 bar. Overall, the observed spatial distributions in entrapment at different pressures suggest that the α-alumina pellets exhibit some degree of pore size correlation on a macroscopic ($>10 \mu m$) scale. In addition, while pore shielding effects can result in inaccuracies in the PSDs normally generated via mercury porosimetry tests, the CXT images shown above

demonstrate how CXT can remove this effect, thereby aiding in mercury porosimetry data interpretation.

5.2.2.2. Throat-pore co-ordination (inter-pore connectivity).

The throat-pore co-ordination number denotes the number of separate routes mercury can take to/from a specific pore during intrusion and retraction. These values can vary at different pore size scales within a pellet (Rigby et al., 2004a,b). Previous studies have shown that lower pore co-ordination numbers result in greater pore shielding of internal pores (Wardlaw and McKellar, 1981; Rigby and Edler, 2002). Given the observed pore shielding and high entrapment, this suggests connectivity between macropores in the pellets is low. In Fig. 15b, all of the percolation pathways are highlighted by entrapped mercury that clearly visible within the image resolution. The mercury threads are often seen to take highly particular, curvilinear paths, suggesting a low number of pore connections on a macroporous level.

5.2.2.3. Pore geometry.

As mentioned in Appendix A, saddle- and annular-shaped mercury ganglia have been observed in the CXT images. Previous work in the literature suggests that these ganglia forms can be explained by higher pore-throat size ratios. Glass micro-model and modelling studies (Wardlaw and McKellar, 1981; Ioannidis and Chatzis, 1993) have shown that the pressure decrease during retraction causes mercury threads within the pores to assume saddle-shaped configurations as they become more unstable. At a certain point the mercury either retreats from the pore or becomes entrapped by snap-off. Larger pore-throat size ratios and geometric disparity between pores have been found to promote snap-off (Rigby et al., 2003) and increase entrapment (Tsakiroglou and Payatakes, 1991) and this appears to occur to some extent in the $> 100\,\mu m$ pore network. Glass micro-model experiments conducted by Wardlaw and McKellar (1981) on models consisting of wide pore bodies joined by narrow necks with a range of different sizes, suggested that the amount of mercury entrapped increased with increased pore-throat size ratio. The annular shape of the entrapped mercury ganglia in Fig. A1(a)–(c) allows the rough volume of the pore to be estimated, and thence the relative fraction of entrapped mercury to be determined ($\sim$30–50%). From a comparison with the model data in images from glass micromodels (Wardlaw and McKellar, 1981), this suggests that the pores were guarded by relatively narrow necks at least $\sim$5–6 times smaller than the pore body.

6. Conclusions

MF-DFT simulations have suggested that, when a particular idiosyncratic form for the top of mercury intrusion and extrusion curves is observed in porosimetry data, it may be associated with a pore network wherein the smallest pores form through interconnections between larger pores, such that mercury menisci completely coalesce within the smaller pores at the top of the intrusion curve. CXT has permitted the pore potential effect to be seen directly by studying mercury entrapment within a model porous material where a mercury-wetting material (Pt) was located in a particular macroscopic region. It was found that mercury entrapment preferentially arose within the region in which the pore potential would have been increased due to the presence of the wetting material. It has also been shown that CXT can be used to directly detect percolation pathways in a macroporous alumina, and study the spatial configurations of entrapped mercury ganglia within such an amorphous material.

Appendix A

A number of the entrapped mercury ganglia appear to be saddle-like, or annular in shape, as opposed to filling the apparent pore spaces fully, as is more clearly visible in Fig. A1(a)–(c).
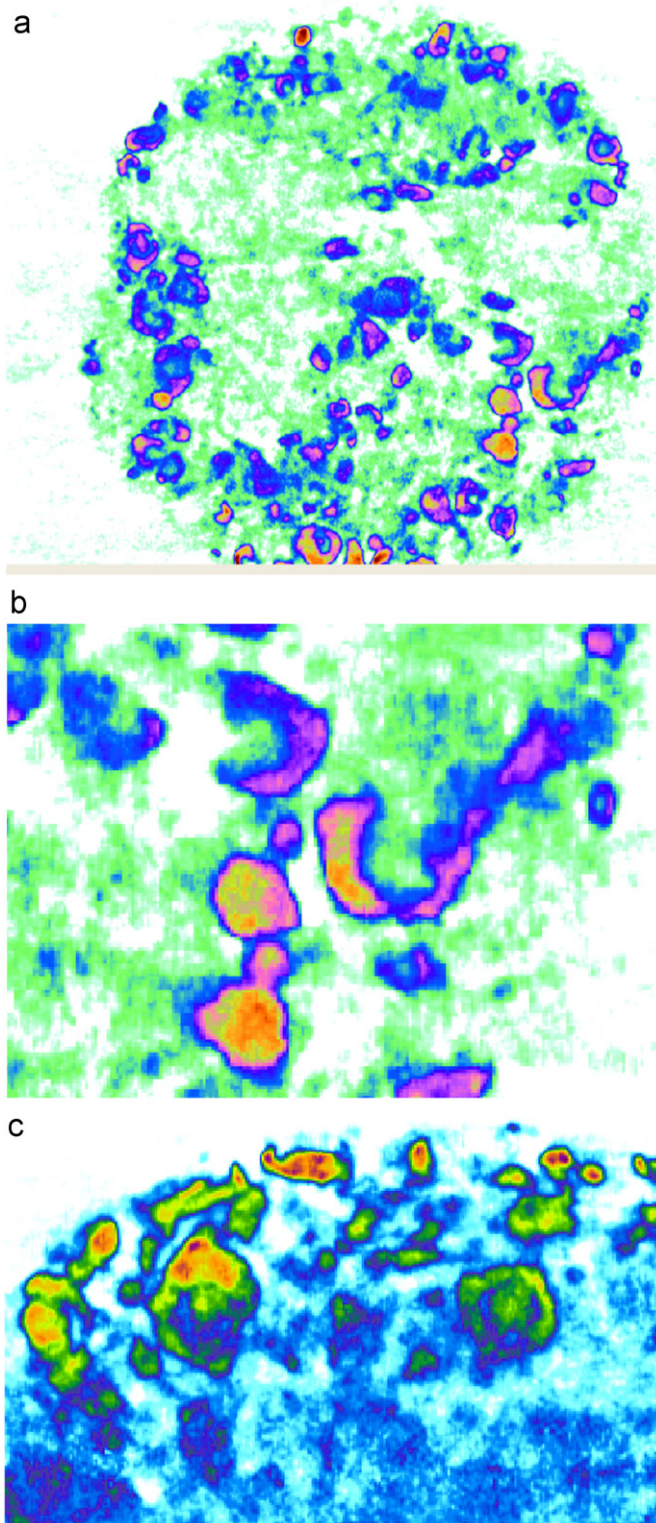

Fig. A1. (a) Processed image of different slice of sample SG2, with close up of entrapped mercury ganglia (b), and (c) close up processed image of mercury ganglia in sample SG3.

References

Androutsopoulos, G.P., Mann, R., 1979. Evaluation of mercury porosimeter experiments using a network pore structure model. Chemical Engineering Science 34, 1203–1212.

Baldwin, C.A., Sederman, A.J., Mantle, M.D., Alexander, P., Gladden, L.F., 1996. Determination and characterization of the structure of a pore space from 3D volume images. Journal of Colloid and Interface Science 181, 79–92.

Bryant, S., Mason, G., Mellor, D., 1996. Quantification of spatial correlation in porous media and its effect on mercury porosimetry. Journal of Colloid and Interface Science 177, 88–100.

Burch, S., 2002. Measurement of density variations in compacted parts using X-ray computerised tomography. MPR Technical Trends, 24–28.

de Paiva, R.F., Lynch, J., Rosenburg, E., Bisiaux, M., 1998. A beam hardening correction for X-ray microtomography. NDT&E International 31, 17–22.

Douarche, N., Rouby, D., Peix, G., Jouin, J.M., 2001. Relations between X-ray tomography, density and mechanical properties in carbon-carbon composites. Carbon 39, 1455–1465.

Giesche, H., 2006. Mercury porosimetry: A general (practical) overview. Particle and Particle Systems Characterisation 23, 9–19.

Gostick, J.T., Ioannidis, M.A., Fowler, M.W., Pritzker, M.D., 2009. Wettability and capillary behavior of fibrous gas diffusion media for polymer electrolyte membrane fuel cells. Journal of Power Sources 194, 433–444.

Holzer, L., Indutnyi, F., Gasser, P.H., Munch, B., Wegmann, M., 2004. Three-dimensional analysis of porous BaTiO$_3$ ceramics using FIB nanotomography. Journal of Microscopy 216, 84–95.

Hyväluoma, J., Raiskinmäki, P., Jäsberg, A., Koponen, A., Kataja, M., Timonen, J., 2004. Evaluation of a lattice-Boltzmann method for mercury intrusion porosimetry simulations. Future Generations Computer Systems 20, 1003–1011.

Ioannidis, M.A., Chatzis, I., 1993. A mixed-percolation model of capillary hysteresis and entrapment in mercury porosimetry. Journal of Colloid and Interface Science 161, 278–291.

Kloubek, J., 1981. Hysteresis in porosimetry. Powder Technology 29, 63–73.

Koster, A.J., Ziese, U., Verklejj, A.J., Janssen, A.H., De Jong, K.P., 2000. Three-dimensional transmission electron microscopy: A novel imaging and characterization technique with nanometre scale resolution for materials science. Journal of Physical Chemistry B 104, 9368–9370.

Liabastre, A.A., Orr, C., 1978. Evaluation of pore structure by mercury penetration. J. Colloid Interface Sci. 64, 1–18.

Libby, B., Monson, P.A., 2004. Adsorption/desorption hysteresis in inkbottle pores: A density functional theory and Monte Carlo simulation study. Langmuir 20, 4289–4294.

Lin C.L., Miller J.D., (2001). A new cone beam X-ray microtomography facility for 3D analysis of multiphase materials. Proceedings of 2nd World Congress on Industrial Process Tomography, Hannover, Germany, August 29–31.

Lowell, S., Shields, J.E., 1982. Influence of pore potential on hysteresis and entrapment in mercury porosimetry–pore potential hysteresis porosimetry. Journal of Colloid and Interface Science 90, 203–211.

Lowell, S., Shields, J.E., 1984. Power Surface Area and Porosity. Chapman and Hall, London.

Matthews, G.P., Ridgway, C.J., Spearing, M.C., 1995. Void space modeling of mercury intrusion hysteresis in sandstone, paper coating and other porous media. Journal of Colloid and Interface Science 171, 8–27.

McCullough, E., 1975. Photon attenuation in computed tomography. Medical Physics 2, 307–320.

Miguélez-Morán, A.M., Wu, C., Dong, H., Seville, J.P.K., 2009. Characterisation of density distributions in roller-compacted ribbons using micro-indentation and X-ray micro-computed tomography. European Journal of Pharmaceuticals and Biopharmaceutics 72, 173–182.

Milburn, D.R., Adkins, B.D., Davis, B.H., 1994. Alumina supported molybdenum and tungsten oxide catalysts. Surface area and pore size distribution from nitrogen adsorption and mercury penetration. Applied Catalysis A: General 119, 205–222.

Mousavi, R., Miri, T., Cox, P.W., Fryer, P.J., 2005. A novel technique for ice-crystal visualisation in frozen solids using X-ray micro-computed tomography. Journal of Food Science 70, 437–442.

Phillips, D.H., Lannutti, J.J., 1997. Measuring physical density with X-ray computed tomography. NDT&E International 30, 339–350.

Porcheron, F., Monson, P.A., 2004. Modelling mercury porosimetry using statistical mechanics. Langmuir 20, 6482–6489.

Porcheron, F., Thommes, M., Ahmad, R., Monson, P.A., 2007. Mercury porosimetry in mersoporous glasses: A comparison of experiments with results from a molecular model. Langmuir 23, 3372–3380.

Portsmouth, R.L., Gladden, L.F., 1992. Mercury porosimetry as a probe of pore connectivity. Transactions of the Institution of Chemical Engineers 70A, 63–70.

Reimann, D.A., Hames, S.M., Flynn, M.J., Fyhrie, D.P., 1997. A cone beam computed tomography system for true 3D imaging of specimens. Applied Radiation and Isotopes 48, 1433–1436.

Rigby, S.P., 2000. A hierarchical structural model for the interpretation of mercury porosimetry and nitrogen sorption. Journal of Colloid and Interface Science 224, 382–396.

Rigby, S.P., 2002. New methodologies in mercury porosimetry. Studies in Surface Science and Catalysis 144, 185–192.

Rigby, S.P., Chigada, P.I., 2010. MF-DFT and experimental investigations of the origins of hysteresis in mercury porosimetry of silica materials. Langmuir 26, 241–248.

Rigby, S.P., Chigada, P.I., Evbuomvan, I.O., Chudek, J.A., Miri, T., Wood, J., Bakalis, S., 2008. Experimental and modelling studies of the kinetics of mercury retraction from highly-confined geometries during porosimetry in the transport and the quasi-equilibrium regimes. Chemical Engineering Science 63, 5771–5788.

Rigby, S.P., Edler, K.J., 2002. The influence of mercury contact angle, surface tension and retraction mechanism on the interpretation of mercury porosimetry data. Journal of Colloid and Interface Science 250, 175–190.

Rigby, S.P., Fletcher, R.S., 2004. Interfacing mercury porosimetry with nitrogen sorption. Particle & Particle Systems Characterisation 21, 138–148.

Rigby, S.P., Fletcher, R.S., Riley, S.N., 2002. Determination of the multiscale percolation properties of porous media using mercury porosimetry. Industrial & Engineering Chemistry Research 41, 1205–1226.

Rigby, S.P., Fletcher, R.S., Riley, S.N., 2003. Determination of the cause of mercury entrapment during porosimetry experiments on sol–gel silica catalyst supports. Applied Catalysis A: General 247, 27–39.

Rigby, S.P., Fletcher, R.S., Riley, S.N., 2004a. Characterisation of porous solids using integrated nitrogen sorption and mercury porosimetry. Chemical Engineering Science 59, 41–51.

Rigby, S.P., Gladden, L.F., 1996. NMR and fractal modelling studies of transport in porous media. Chemical Engineering Science 51, 2263–2272.

Rigby, S.P., Watt-Smith, M.J., Fletcher, R.S., 2004b. Simultaneous determination of the pore-length distribution and pore connectivity for porous catalyst supports using integrated nitrogen sorption and mercury porosimetry. Journal of Catalysis 227, 68–76.

Skyscan, Co., 2003. T View: Visualisation, Alteration, Cut, Measurements User Manual. Aartselaar, Belgium: Skyscan Co. Available from ⟨www.skyscan.be⟩. Accessed Feb. 2009.

Thommes, M., Skudas, R., Unger, K.K., Lubda, D., 2008. Textural characterization of native and n-alkyl bonded silica monoliths by mercury intrusion/extrusion, inverse size exclusion chromatography and nitrogen adsorption. Journal of Chromatography A 1191, 57–66.

Tsakiroglou, C.D., Payatakes, A.C., 1991. Effects of pore-size correlations on mercury porosimetry curves. Journal of Colloid and Interface Science 146, 479–494.

Van Brakel, J., Modry, S., Svata, M., 1981. Mercury porosimetry: State of the art. Powder Technology 29, 1–12.

Wardlaw, N.C., McKellar, M., 1981. Mercury porosimetry and the interpretation of pore geometry in sedimentary rocks and artificial models. Powder Technology 29, 127–143.

Washburn, E.W., 1921. The dynamics of capillary flow. Physical Review 17, 273–283.

Zhu, S.-B., 1995. Interactions of water, ions and atoms with metal surfaces. Surface Science 329, 276–284.